

AXISYMMETRIC AB INITIO CORE-COLLAPSE SUPERNOVA SIMULATIONS OF 12–25 M_{\odot} STARS

STEPHEN W. BRUENN¹, ANTHONY MEZZACAPPA^{2,3,4}, W. RAPHAEL HIX^{2,3}, ERIC J. LENTZ^{3,2,5}, O. E. BRONSON MESSER^{6,3,4},
 ERIC J. LINGERFELT^{2,4}, JOHN M. BLONDIN⁷, EIRIK ENDEVE⁴, PEDRO MARRONETTI^{8,1}, AND KONSTANTIN N. YAKUNIN¹

¹ Department of Physics, Florida Atlantic University, 777 Glades Road, Boca Raton, FL 33431-0991, USA; bruenn@fau.edu

² Physics Division, Oak Ridge National Laboratory, P.O. Box 2008, Oak Ridge, TN 37831-6354, USA

³ Department of Physics and Astronomy, University of Tennessee, Knoxville, TN 37996-1200, USA

⁴ Computer Science and Mathematics Division, Oak Ridge National Laboratory, P.O. Box 2008, Oak Ridge, TN 37831-6164, USA

⁵ Joint Institute for Heavy Ion Research, Oak Ridge National Laboratory, P.O. Box 2008, Oak Ridge, TN 37831-6374, USA

⁶ National Center for Computational Sciences, Oak Ridge National Laboratory, P.O. Box 2008, Oak Ridge, TN 37831-6164, USA

⁷ Department of Physics, North Carolina State University, Raleigh, NC 27695-8202, USA

⁸ Physics Division, National Science Foundation, Arlington, VA 22207, USA

Received 2012 December 7; accepted 2013 February 18; published 2013 March 25

ABSTRACT

We present an overview of four ab initio axisymmetric core-collapse supernova simulations employing *detailed* spectral neutrino transport computed with our CHIMERA code and initiated from Woosley & Heger progenitors of mass 12, 15, 20, and 25 M_{\odot} . All four models exhibit shock revival over ~ 200 ms (leading to the possibility of explosion), driven by neutrino energy deposition. Hydrodynamic instabilities that impart substantial asymmetries to the shock aid these revivals, with convection appearing first in the 12 M_{\odot} model and the standing accretion shock instability appearing first in the 25 M_{\odot} model. Three of the models have developed pronounced prolate morphologies (the 20 M_{\odot} model has remained approximately spherical). By 500 ms after bounce the mean shock radii in all four models exceed 3000 km and the diagnostic explosion energies are 0.33, 0.66, 0.65, and 0.70 Bethe ($B = 10^{51}$ erg) for the 12, 15, 20, and 25 M_{\odot} models, respectively, and are increasing. The three least massive of our models are already sufficiently energetic to completely unbind the envelopes of their progenitors (i.e., to explode), as evidenced by our best estimate of their explosion energies, which first become positive at 320, 380, and 440 ms after bounce. By 850 ms the 12 M_{\odot} diagnostic explosion energy has saturated at 0.38 B, and our estimate for the final kinetic energy of the ejecta is ~ 0.3 B, which is comparable to observations for lower mass progenitors.

Key words: neutrinos – radiative transfer – supernovae: general

Online-only material: color figures, animation

1. INTRODUCTION

Colgate & White (1966) originated the idea that core-collapse supernovae (CCSNe) may be neutrino-driven. Because realistically modeling CCSNe is a computationally complex task of tying together hydrodynamics, neutrino transport, general relativity (GR), nuclear burning, and a realistic equation of state (EoS), and since the many feedbacks and the nonlinearity of the process preclude an analytical treatment, progress in the field has been closely tied to advances in computational resources and code development (Mezzacappa 2005; Kotake et al. 2006; Janka 2012). Two decades ago advances of this sort made possible the first generation of CCSNe simulations in two dimensions (2D; Herant et al. 1994; Burrows et al. 1995; Janka & Müller 1996; Mezzacappa et al. 1998; Fryer & Warren 2002). These simulations, by allowing, among other things, neutrino-driven convection below the shock and continued accretion and shock expansion to coexist, gave explosions. In contrast, continually refined spherically symmetric CCSNe simulations failed to explode except for the lightest progenitors (Rampp & Janka 2000; Mezzacappa et al. 2001; Liebendörfer et al. 2001, 2004; Buras et al. 2003). Further investigation has shown the crucial importance of multidimensional effects, including the standing accretion shock instability (SASI; Blondin et al. 2003), in shaping explosions, and in accounting for the many observed CCSNe explosion asymmetries (see, e.g., Janka 2012).

While the first-generation 2D CCSNe simulations were limited by their use of gray neutrino transport or precomputed spectral neutrino transport, current computing resources have

permitted second-generation 2D CCSNe simulations with self-consistent, spectral neutrino transport (Buras et al. 2003, 2006a, 2006b; Burrows et al. 2006, 2007; Bruenn et al. 2006, 2009; Marek & Janka 2009; Suwa et al. 2010; Takiwaki et al. 2012; Müller et al. 2012b, 2012a), essential for accurately computing the neutrino–matter coupling at the heart of the neutrino-driven CCSN mechanism. Realistic multidimensional ab initio (neutrino luminosities and spectra computed from *detailed* spectral neutrino transport rather than prescribed, parameterized, or incomplete spectral transport) CCSNe simulations are essential for elucidating the details of the neutrino-driven supernova mechanism and fully accounting for supernova observables, including explosion energies, neutrino and gravitational wave signatures, nucleosynthesis, compositional mixing, and neutron star recoils. The Garching group has published such simulations in axisymmetry using the Vertex code, incorporating a complete set of neutrino opacities, velocity-dependent transport terms, and neutrino-energy-bin coupling in the neutrino transport, standard EoSs, and GR corrections to Newtonian self-gravity (Buras et al. 2006a, 2006b; Marek & Janka 2009) or the conformal flatness GR approximation (Müller et al. 2012a, 2012b; see Janka et al. 2012; Müller et al. 2013 for an overview). Their successful models either produce weak explosions or were reported before their explosion energies saturated.

The limited number of published ab initio CCSNe simulations with detailed neutrino transport, the quantitative differences we obtain relative to the Garching group, and the specifics of our findings (explosions more broadly consistent with observations) motivate us to present in this Letter an outline of four simulations

being performed with our CHIMERA code. These simulations span progenitors of mass 12–25 M_{\odot} with details comparable to Marek & Janka (2009). Here we describe some of the general features already manifested in our simulations and how they support the viability of the neutrino-driven CCSN mechanism.

2. NUMERICAL METHODS AND INPUTS

CHIMERA is a parallel, multi-physics code built specifically for multidimensional simulation of CCSNe. It is a combination of separate codes for hydrodynamics and gravity; neutrino transport and opacities; and nuclear EoS and reaction network, coupled by a layer that oversees data management, parallelism, I/O, and control. The hydrodynamics are evolved via a dimensionally split, Lagrangian-remap (PPMLR) scheme (Colella & Woodward 1984) as implemented in VH1 (Hawley et al. 2012). Self-gravity is computed by multipole expansion (Müller & Steinmetz 1995) replacing the Newtonian monopole with a GR monopole (Marek et al. 2006, Case A). Neutrino transport is computed in the “ray-by-ray-plus” (RbR+) approximation (Buras et al. 2003), where an independent, spherically symmetric transport solve is computed for each angular “ray” (θ -zone). Neutrinos are advected laterally (in the θ -direction) with the fluid and contribute to the lateral pressure gradient where $\rho > 10^{12} \text{ g cm}^{-3}$. The transport solver is an improved and updated version of the multi-group, flux-limited, diffusion transport solver of Bruenn (1985), enhanced for GR (Bruenn et al. 2001), with an additional geometric flux limiter to prevent the over-rapid transition to free streaming of the standard flux limiter. All $O(v/c)$ observer corrections have been included. We solve for all three flavors of (anti-)neutrinos with four coupled species: $\nu_e, \bar{\nu}_e, \nu_{\mu\tau} = \{\nu_{\mu}, \nu_{\tau}\}, \bar{\nu}_{\mu\tau} = \{\bar{\nu}_{\mu}, \bar{\nu}_{\tau}\}$, with 20 energy groups each for $\alpha\epsilon = 4\text{--}250 \text{ MeV}$, where α is the lapse function and ϵ the comoving-frame group-center energy. The neutrino–matter interactions include emission, absorption, and non-isoenergetic scattering on free nucleons (Reddy et al. 1998) with weak magnetism corrections (Horowitz 2002); emission/absorption (electron capture) on nuclei (Langanke et al. 2003); isoenergetic scattering on nuclei, including ion–ion correlations; non-isoenergetic scattering on electrons and positrons; and pair emission from e^+e^- -annihilation (Bruenn 1985) and nucleon–nucleon bremsstrahlung (Hannestad & Raffelt 1998). Unlike the Garching group, we do not include the effective mass corrections at high density or the $\nu_e\bar{\nu}_e \rightarrow \nu_{\mu\tau}\bar{\nu}_{\mu\tau}$ process. We utilize the $K = 220 \text{ MeV}$ incompressibility version of the Lattimer & Swesty (1991) EoS for $\rho > 10^{11} \text{ g cm}^{-3}$ and a modified version of the Cooperstein (1985) EoS for $\rho < 10^{11} \text{ g cm}^{-3}$ where nuclear statistical equilibrium (NSE) applies. To aid the transition to the XNet (Hix & Thielemann 1999) 14-species α -network ($\alpha, {}^{12}\text{C}\text{--}{}^{60}\text{Zn}$) used for the non-NSE regions, we have constructed a 17-species NSE solver to be used in place of the Cooperstein EoS for $Y_e > 0.46$. An extended version of the Cooperstein electron–photon EoS is used throughout.

During evolution the radial zones are gradually and automatically repositioned during the remap step to track changes in the radial structure. To minimize restrictions on the time step from the Courant limit, we “freeze” the lateral hydrodynamics for the inner eight zones during collapse, and, after prompt convection fades, we expand the laterally frozen region to the inner 8–10 km. In the “frozen” region we set $v_{\theta} = 0$ and skip the lateral hydrodynamic sweep. The full radial hydrodynamics and neutrino transport are always computed to the center of the simulation for all angular rays. A more extensive description of CHIMERA is under preparation.

Four non-rotating axisymmetric models (designated B12-WH07, B15-WH07, B20-WH07, and B25-WH07, corresponding to progenitor masses of 12, 15, 20, and 25 M_{\odot}), and identical one-dimensional (1D) models, are initialized without artificial perturbation from the pre-supernova progenitors of Woosley & Heger (2007). A grid of 512 non-equally spaced radial zones covers from the stellar center into the oxygen-rich layers. The 2D models employ 256 uniform-sized angular zones from 0 to π .

3. RESULTS

All 2D models experience similar evolution during collapse and immediately after bounce. Theta velocities of a few cm s^{-1} develop by bounce, most likely from numerical roundoff. These grow to at most $\sim 10 \text{ km s}^{-1}$ and $\sim 100 \text{ km s}^{-1}$ in the pre-shock and post-shock regions, respectively, at a post-bounce time, t_{pb} , of 10 ms. At $t_{\text{pb}} \sim 2 \text{ ms}$ the shock breaks through the ν_e -sphere, initiating a rapid deleptonization front whose inner edge advects inward with the fluid. An unstable lepton gradient results, which is stabilized by the positive entropy gradient laid down by the shock as it initially strengthens. The initial oscillations of the proto-neutron star (PNS) periodically strengthen and weaken the shock, causing entropy-unstable pockets and transient convective episodes behind the shock. By $t_{\text{pb}} \sim 12 \text{ ms}$ an extended unstable entropy gradient has developed behind the shock as it weakens, extending down to $\sim 60 \text{ km}$ and driving a brief episode of convection (Figure 1; 12 ms panel). This episode of “prompt” convection has little appreciable effect on the shock, and by $t_{\text{pb}} \sim 40 \text{ ms}$ convective activity has ceased.

Up to $t_{\text{pb}} \sim 100 \text{ ms}$, the shock trajectories of corresponding 1D and 2D models track each other closely (Figure 2; lower panel). Remarkably, the shock trajectories for different progenitors track each other rather closely as well. This is a consequence of the compensating factors that determine the radius of the shock during its quasi-stationary accretion phase. Referring to Equation (1) of Janka (2012), these factors (graphed for B12-WH07 and B25-WH07 in Figure 3; upper panel) are the PNS radius and the ν -sphere temperature, whose increase increases the shock radius, and the PNS mass and the mass accretion rate at the shock whose increase has the opposite effect. Despite the variations of these factors, their combinations during the quasi-stationary accretion phase (Figure 3; upper panel, solid lines) are quite similar.

At $t_{\text{pb}} \sim 100 \text{ ms}$ several evolutionary developments occur in all 2D models, causing the shock trajectories of the 1D and 2D models to diverge. First, the ratio of τ_{adv} , the advection timescale through the gain region (region of positive net neutrino heating below the shock), to τ_{conv} , the Brunt–Väisälä convective growth timescale, begins to exceed the critical value $\tau_{\text{adv}}/\tau_{\text{conv}} \gtrsim 3$ (Foglizzo et al. 2006). Convection in the gain region begins (Figure 1; 90 ms panel), driven by neutrino heating and seeded by the prompt convection episode. Neutrino-driven convection pushes the shock out, enlarging the gain region and increasing τ_{adv} . Second, the ratio of τ_{adv} to τ_{heat} (ratio of the thermal energy E_{th} to the net neutrino heating rate \dot{Q}_{ν_e} in the gain region) begins to exceed unity. (Using the total energy rather than E_{th} to compute τ_{heat} increases by $\sim 30\%$ the time from bounce for $\tau_{\text{adv}}/\tau_{\text{heat}}$ to exceed unity.) This signals the beginning of rising entropy in the gain region and an eventual shock revival (Buras et al. 2006a; Thompson et al. 2005). Third, the SASI begins to manifest through low-mode distortions of the shock and oscillating patterns of the radial velocity (evident

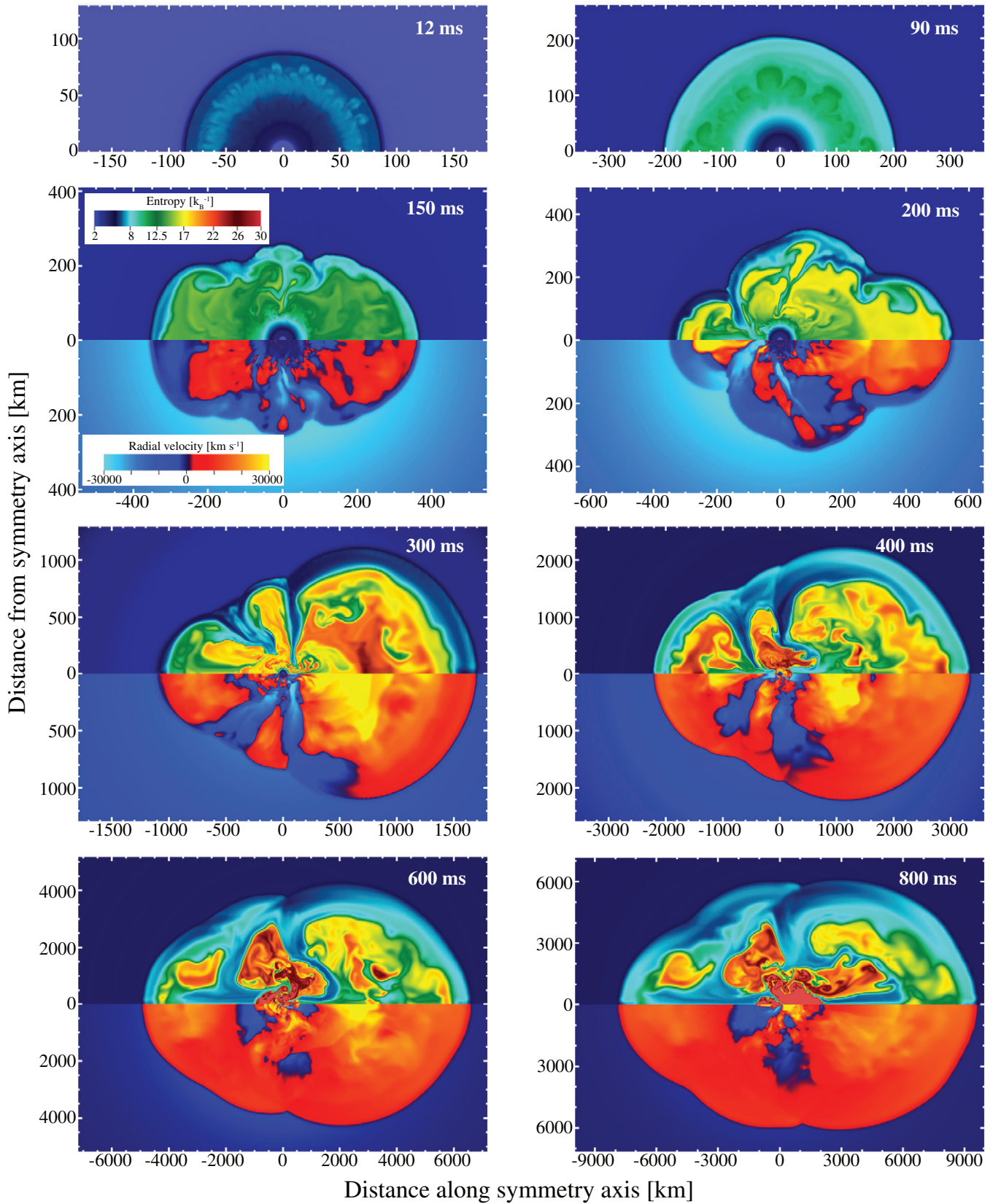


Figure 1. Evolution of the entropy (upper half) and radial velocity (lower half) for B12-WH07, with snapshots at $t_{\text{pb}} = 12, 90, 150, 200, 300, 400, 600,$ and 800 ms. The scale grows in time to capture the expansion of the supernova shockwave, but the color maps remain constant. The radial velocity portion is omitted for the first two snapshots.

(An animation of this figure is available in the online journal.)

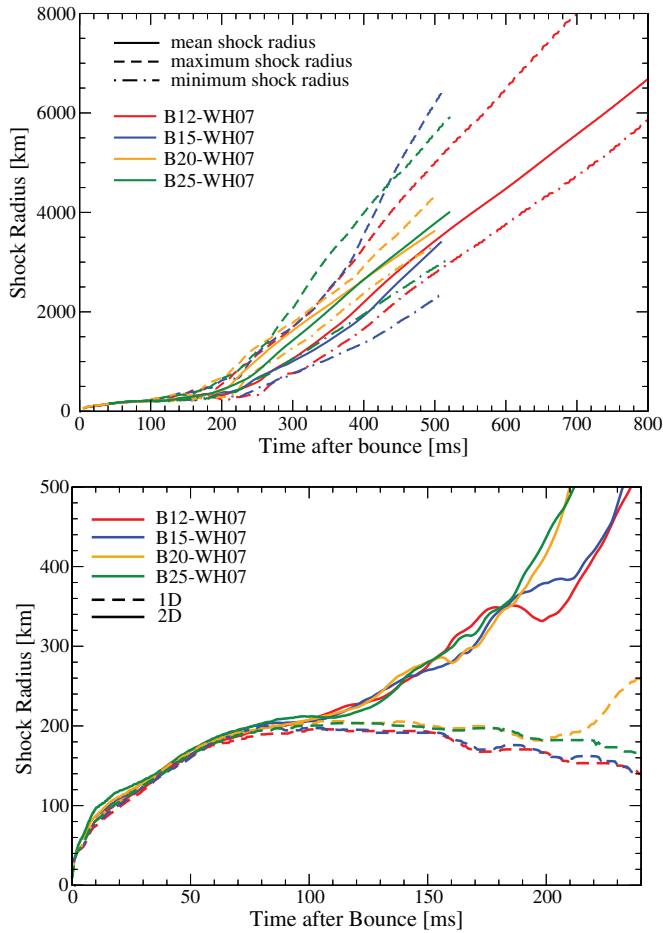


Figure 2. Upper panel: mean, minimum, and maximum shock radii vs. t_{pb} for all simulations. Lower panel: mean shock radii for all simulations and their 1D equivalents.

(A color version of this figure is available in the online journal.)

in the animated version of Figure 1), causing, for example, the gain region to swell along the poles and contract in the equatorial regions (Figure 1; 150 ms panel). This distortion mode increases τ_{adv}/τ_{heat} in the expanded regions and decreases it in the contracted regions creating outflow plumes and inflow funnels in the former and latter regions, respectively. Thus, while the shocks of the 1D models slowly contract after $t_{pb} \sim 100$ ms, the average shock radii of the 2D models continue to slowly increase. The expansion accelerates after $t_{pb} \sim 200$ ms (Figure 2).

Going from B12-WH07 to B25-WH07, \dot{Q}_{ν_e} increases ~ 2 – 2.5 fold, E_{th} increases ~ 1.5 fold, and τ_{adv} decreases ~ 1.5 fold, consequently $\tau_{adv}/\tau_{heat} \gtrsim 1$ at about the same t_{pb} for all four models. On the other hand, the decrease in τ_{adv} noticeably delays the onset of neutrino-driven convection in the more massive models—from $t_{pb} \sim 60$ ms (B12-WH07) to $t_{pb} \sim 100$ ms (B25-WH07). Consequently, it appears that neutrino-driven convection precedes the SASI in B12-WH07 but follows it in the B25-WH07, the SASI having time to saturate in the latter model before the onset of convection (cf. Müller et al. 2012a). B15-WH07 and B20-WH07 are intermediate cases and precedence of convection or the SASI is not clear.

A Legendre decomposition of the shock deformation (computed per Blondin & Mezzacappa 2006) indicates that the growth of the SASI is dominated by the $l = 2$ (quadrupolar) mode in B12-WH07 and B15-WH07, while the $l = 1$ (dipolar)

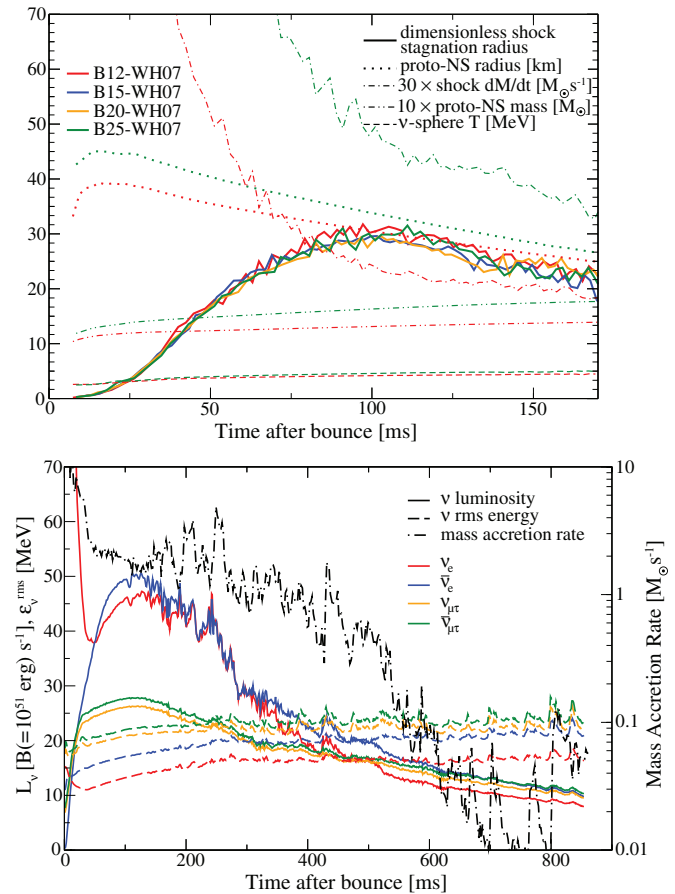


Figure 3. Upper panel: analytic shock using Equation (1) of Janka (2012; solid lines, dimensionless) for all simulations; and PNS radii ($\rho = 10^{11} \text{ g cm}^{-3}$ surface; dotted, km), $30 \times dM/dt$ at shock (dash-dotted, $M_\odot s^{-1}$), PNS mass (double-dot-dashed, $0.1 M_\odot$), and v-sphere temperature (dashed, MeV) for the extreme cases, B12-WH07 and B25-WH07. Lower panel: luminosity (solid lines, $B s^{-1}$) and comoving-frame rms energies (dashed, MeV) for all species of neutrinos, and mass accretion rate onto the PNS (dot-dashed, $M_\odot s^{-1}$) for B12-WH07.

(A color version of this figure is available in the online journal.)

mode is dominant in B20-WH07 and B25-WH07. The subsequent rise in the amplitude of shock deformation as the shock begins to accelerate outward is always dominated by the $l = 1$ mode. The shock deformation oscillates, with a period increasing with the progenitor mass, from 18 ms for B12-WH07 to 30 ms for B25-WH07, though period variations are seen in each model.

The neutrino luminosities L_ν and rms energies $\langle E_\nu \rangle_{rms}$ for all models follow a similar pattern to that of B12-WH07 (Figure 3; lower panel). Following the ν_e -break-out burst, the luminosities of all neutrino species peak between 100 and 200 ms. The ν_e -, $\bar{\nu}_e$ -luminosities, which arise both from the core and from the energy released by accreting matter, exhibit a more pronounced peak during the peak of the mass accretion rate than $L_{\nu_{\mu\tau}}$ and $L_{\bar{\nu}_{\mu\tau}}$, which arise more exclusively from the core. After 200 ms there is a rapid falloff in L_{ν_e} and $L_{\bar{\nu}_e}$ as the shock begins to accelerate outward and the mass accretion rate declines. $\langle E_\nu \rangle_{rms}$ follows the usual hierarchy, with energy increasing from ν_e to $\bar{\nu}_e$ to $\nu_{\mu\tau}$ to $\bar{\nu}_{\mu\tau}$, the latter three becoming separated by only a few MeV after several hundred ms. The split between $\langle E_{\nu_{\mu\tau}} \rangle_{rms}$ and $\langle E_{\bar{\nu}_{\mu\tau}} \rangle_{rms}$ is due to weak magnetism, which increases (decreases) the opacities of $\nu_{\mu\tau}$ ($\bar{\nu}_{\mu\tau}$). Weak magnetism also causes the $\bar{\nu}_e$ -luminosity to exceed the ν_e -luminosity at times after bounce

Table 1
Model Summary Table

Property	Models			
	B12-WH07	B15-WH07	B20-WH07	B25-WH07
Progenitor mass, $M_{\text{ZAMS}} (M_{\odot})$	12	15	20	25
Progenitor compactness, $\xi_{1.75}$	0.234	0.598	1.10	1.25
Initial simulation domain radius (km)	30000	20000	20000	20000
Simulation enclosed mass (M_{\odot})	2.08	2.75	3.51	4.57
Radial zone count	512	512	512	512
Angular zone count	256	256	256	256
Collapse time (initiation to bounce; ms)	266	335	462	470
Bounce, central density ($10^{14} \text{ g cm}^{-3}$)	3.13	3.45	3.42	3.29
Bounce, central Y_e	0.240	0.249	0.248	0.246
Bounce, shock position (M_{\odot})	0.45	0.46	0.47	0.47
Time to growth in gain region mass, t_{gain} (ms)	256	221	195	192
Time to positive diagnostic energy $> 0.01 \text{ B}$ (ms)	219	207	192	197
Time to mean shock radius of 500 km, t_{500} (ms)	236	233	208	212
Post-bounce epoch, t_{pb} (ms)	850	500	500	500
Post-bounce diagnostic energy, E^+ (B)	0.38	0.33	0.66	0.70
Post-bounce E_{ov}^+ (B; see the text)	0.29	0.0.19	0.27	0.03
Post-bounce $E_{\text{ov,rec}}^+$ (B; see the text)	0.32	0.23	0.41	0.08
Post-bounce mean shock radius (km)	7245	3429	3293	3632
Post-bounce shock deformation, d_{shock}	0.42	0.31	0.52	0.027
Post-bounce PNS rest mass (M_{\odot})	1.48	1.48	1.66	1.80

for this model, though the ν_e number luminosity is always dominant. $\langle E_{\nu} \rangle_{\text{rms}}$ for all neutrino species increases slowly as the ν -spheres contract and heat along with the PNS.

Progenitor masses are correlated with the compactness parameter of O'Connor & Ott (2011; see Table 1), and the luminosities of all neutrino flavors increase with this parameter, nearly doubling from B12-WH07 to B25-WH07 between 50 and 250 ms after bounce. $\langle E_{\nu} \rangle_{\text{rms}}$, however, shows only a small increase (a few MeV) with compactness. These trends can be attributed to the dependence of the luminosity on $R_{\nu\text{-sph}}^2 T_{\nu\text{-sph}}^4$ and the dependence of the $\langle E_{\nu} \rangle_{\text{rms}}$ only on $T_{\nu\text{-sph}}$, where $R_{\nu\text{-sph}}$ and $T_{\nu\text{-sph}}$ are radius and temperature of the ν -sphere, both of which increase with the progenitor compactness during the accretion shock phase (Figure 3, upper panel; note $R_{\nu\text{-sph}} \propto R_{\text{PNS}}$).

For all the models, L_{ν} and $\langle E_{\nu} \rangle_{\text{rms}}$ are initially isotropic. By $t_{\text{pb}} = 60 \text{ ms}$ and $t_{\text{pb}} = 100 \text{ ms}$ for the lower and higher mass models, respectively, anisotropies $\sim 10\%$ in $L_{\nu_e, \bar{\nu}_e}$ appear on an $l \sim 10$ scale, the scale of the entropy-driven convection appearing for these models at that time. The L_{ν_e} ($L_{\bar{\nu}_e}$) maxima are anti-correlated (correlated) with the convective plumes, the plumes having higher entropy but lower electron fraction (higher positron density). By $t_{\text{pb}} = 120 \text{ ms}$ anisotropies exist at the $\sim 30\%$ level in all models on a scale of $l = 2-3$, with L_{ν_e} and $L_{\bar{\nu}_e}$ maxima becoming more correlated with each other and with the convective plumes and accretion funnels that frequently curve beneath them. By $t_{\text{pb}} = 200 \text{ ms}$ and thereafter there is a strong $l = 1$ and $l = 2$ component in the $L_{\nu_e, \bar{\nu}_e}$ anisotropy, again correlated with the morphology of the expanding hot plumes and accretion funnels (Figure 1; bottom four panels). $L_{\nu_{\mu\tau}, \bar{\nu}_{\mu\tau}}$ remain quite isotropic up to 200 ms after bounce, but follow, with smaller amplitude, the anisotropic pattern of $L_{\nu_e, \bar{\nu}_e}$ thereafter.

At $t_{\text{pb}} \sim 200 \text{ ms}$ several parameters indicate imminent shock revival and the onset of explosion for each model. First, around this time (noted as t_{gain} in Table 1), the mass residing in the gain region begins to rapidly increase, which increases τ_{adv} and heating efficiency (Janka 2001; Murphy & Burrows 2008; Marek & Janka 2009; Hanke et al. 2012). Second, the $\tau_{\text{adv}}/\tau_{\text{heat}}$

rises significantly above unity around this time, signaling shock revival (Buras et al. 2006a; Thompson et al. 2005). Third, near this time, the mean shock radius exceeds 500 km (denoted t_{500} in Table 1).

A useful parameter characterizing the morphology of the expanding shock is the shock deformation parameter,

$$d_{\text{shock}} = \frac{\max(r_{\text{shock}}(\theta) \cos \theta) - \min(r_{\text{shock}}(\theta) \cos \theta)}{2 \times \max(r_{\text{shock}}(\theta) \sin \theta)} - 1 \quad (1)$$

(Scheck et al. 2006), where $r_{\text{shock}}(\theta)$ is the shock radius as a function of the polar angle, θ . Prolate, oblate, and spherical shocks have positive, negative, and vanishing values of d_{shock} , respectively. Values of d_{shock} for the models at $t_{\text{pb}} = 500 \text{ ms}$ (Table 1) indicate that the shock in three models is significantly prolate while for B20-WH07 it is nearly spherical (see also Figure 2, upper panel).

A measure of the explosion energy frequently used is the diagnostic energy, E^+ (integral of total energy = kinetic + internal + gravitational, where positive; Buras et al. 2006a; Suwa et al. 2010; Müller et al. 2012b). In Figure 4 we show E^+ for our models, as well as two other measures of the explosion energy: $E_{\text{ov}}^+ = E^+ + \text{overburden}$, and $E_{\text{ov,rec}}^+ = E_{\text{ov}}^+ + \text{recombination energy}$. The overburden is the total energy of all negative energy zones on the grid above the innermost positive energy zones plus the total energy of the off-grid material; the recombination energy is the energy that would be released if all ^4He and neutron-proton pairs recombined to ^{56}Ni in the positive total energy zones. We expect that E_{ov}^+ and $E_{\text{ov,rec}}^+$ bound the eventual observable explosion energy from below and above, respectively.

At 500 ms all three explosion energy measures are positive, and increasing, for B12-WH07, B15-WH07, and B20-WH07, but only E^+ is positive for B25-WH07 due to its large off-grid binding energy of -0.655 B . For B12-WH07 at 850 ms, the post-shock velocities exceed escape velocity over one-quarter of the shock surface; the accretion rate onto the PNS is essentially zero; and the model is beginning to transit from the simultaneous

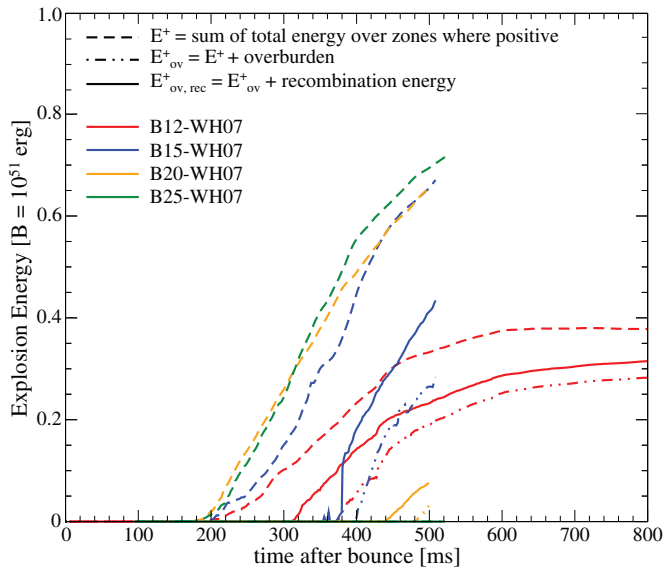


Figure 4. Diagnostic energy (E^+ ; dashed lines) vs. t_{pb} for all simulations. Dash-dotted lines (E^+_{ov}) include binding energy of overburden and dashed lines ($E^+_{ov,rec}$) also include estimated energy gain from nuclear recombination to ^{56}Ni (see definitions in the text).

(A color version of this figure is available in the online journal.)

accretion and outflow phase to the wind phase. The B12-WH07 explosion energies at 850 ms are $E^+ = 0.38$ B, $E^+_{ov} = 0.285$ B, and $E^+_{ov,rec} = 0.32$ B and appear to be leveling off. These energies are broadly consistent with observations for lower mass progenitors (Smartt 2009).

4. DISCUSSION

We have presented results of ab initio axisymmetric CCSN simulations with *detailed* spectral neutrino transport for a suite of four non-rotating models spanning the mass range $12\text{--}25 M_{\odot}$, through $t_{pb} = 500$ ms for B15-WH07, B20-WH07, and B25-WH07, and $t_{pb} = 850$ ms for B12-WH07. At 500 ms, all models show clear indications of developing neutrino-driven explosions, aided initially by strong convective and SASI activity, which imparts pronounced prolate shock deformations in B12-WH07, B15-WH07, and B25-WH07, indicating that large explosion asymmetries are probable (in agreement with observation).

The development of explosions in these models, taking 208–236 ms for the mean shock to reach 500 km, is much slower than in older models—for example, the delayed model of Wilson used by Woosley et al. (1994), for which $t_{500} \sim 150$ ms, or the 2D gray neutrino transport models of Herant et al. (1994), for which $t_{500} \sim 75$ ms. The explosion development times of the CHIMERA models reported here are comparable to those of the Garching group for their models that use modern progenitors ($t_{500} \sim 250$ ms for model G11 from Müller et al. 2012b and $t_{500} \sim 230$ ms for model s27 from Müller et al. 2012a), but significantly shorter than for their models that use older progenitors ($t_{500} \sim 600$ ms for model G15 of Müller et al. 2012b). This suggests a significant progenitor dependence, which makes detailed comparisons difficult. The most pronounced difference between our models and those of the Garching group is the growth of the explosion energy. For example, once the explosion develops, E^+ for both their G15 and s27 models (Janka et al. 2012) grow at a rate of $\sim 0.5 \text{ B s}^{-1}$, a quarter of the rate in our model B15-WH07. The diagnostic

energy in the G11 model saturates at $E^+ \sim 0.03$, one-tenth of the value of our model B12-WH07. Future simulations with both groups using identical progenitors will help elucidate the source of these differences.

Final conclusions regarding the viability of the neutrino-driven CCSN mechanism must wait until different groups obtain similar results from detailed ab initio simulations initiated from the same progenitors and carried out in three dimension. Our simulations thus far support the viability of the neutrino-driven supernova mechanism for the lower progenitor masses and are consistent with observations. These simulations are continuing, and we will publish more complete analyses as they complete.

We thank H.-Th. Janka and B. Müller for a very careful reading of this manuscript and helpful comments. This research was supported by the U.S. Department of Energy Offices of Nuclear Physics and Advanced Scientific Computing Research; the NASA Astrophysics Theory and Fundamental Physics Program (grants NNH08AH71I and NNH11AQ72I); and the National Science Foundation PetaApps Program (grants OCI-0749242, OCI-0749204, and OCI-0749248). This research was also supported by the NSF through TeraGrid resources provided by the National Institute for Computational Sciences under grant number TG-MCA08X010; resources of the National Energy Research Scientific Computing Center, supported by the US DoE Office of Science under Contract No. DE-AC02-05CH11231; and an award of computer time from the Innovative and Novel Computational Impact on Theory and Experiment (INCITE) program at the Oak Ridge Leadership Computing Facility, supported by the US DoE Office of Science under Contract No. DE-AC05-00OR22725.

REFERENCES

- Blondin, J. M., & Mezzacappa, A. 2006, *ApJ*, **642**, 401
- Blondin, J., Mezzacappa, A., & DeMarino, C. 2003, *ApJ*, **584**, 971
- Bruenn, S. W. 1985, *ApJS*, **58**, 771
- Bruenn, S. W., De Nisco, K. R., & Mezzacappa, A. 2001, *ApJ*, **560**, 326
- Bruenn, S. W., Dirk, C. J., Mezzacappa, A., et al. 2006, *JPhCS*, **46**, 393
- Bruenn, S. W., Mezzacappa, A., Hix, W. R., et al. 2009, *JPhCS*, **180**, 012018
- Buras, R., Janka, H.-T., Rampp, M., & Kifonidis, K. 2006a, *A&A*, **457**, 281
- Buras, R., Rampp, M., Janka, H.-T., & Kifonidis, K. 2003, *PhRvL*, **90**, 241101
- Buras, R., Rampp, M., Janka, H.-T., & Kifonidis, K. 2006b, *A&A*, **447**, 1049
- Burrows, A., Hayes, J., & Fryxell, B. A. 1995, *ApJ*, **450**, 830
- Burrows, A., Livne, E., Dessart, L., Ott, C. D., & Murphy, J. 2006, *ApJ*, **640**, 878
- Burrows, A., Livne, E., Dessart, L., Ott, C. D., & Murphy, J. 2007, *ApJ*, **655**, 416
- Colella, P., & Woodward, P. 1984, *JCoPh*, **54**, 174
- Colgate, S. A., & White, R. H. 1966, *ApJ*, **143**, 626
- Cooperstein, J. 1985, *NuPhA*, **438**, 722
- Foglizzo, T., Scheck, L., & Janka, H.-T. 2006, *ApJ*, **652**, 1436
- Fryer, C. L., & Warren, M. S. 2002, *ApJL*, **574**, L65
- Hanke, F., Marek, A., Mueller, B., & Janka, H.-T. 2012, *ApJ*, **755**, 138
- Hannestad, S., & Raffelt, G. 1998, *ApJ*, **507**, 339
- Hawley, J., Blondin, J., Lindahl, G., & Lufkin, E. 2012, *Astrophysics Source Code Library*, **1204.007**
- Herant, M., Benz, W., Hix, W. R., Fryer, C. L., & Colgate, S. A. 1994, *ApJ*, **435**, 339
- Hix, W. R., & Thielemann, F.-K. 1999, *ApJ*, **511**, 862
- Horowitz, C. J. 2002, *PhRvD*, **65**, 43001
- Janka, H.-T. 2001, *A&A*, **368**, 527
- Janka, H.-T. 2012, *ARNPS*, **62**, 407
- Janka, H.-T., Hanke, F., Huedepohl, L., et al. 2012, *PTEP*, **2012**, 010000
- Janka, H.-T., & Müller, E. 1996, *A&A*, **306**, 167
- Kotake, K., Sato, K., & Takahashi, K. 2006, *RPPH*, **69**, 971
- Langanke, K., Martínez-Pinedo, G., Sampaio, J. M., et al. 2003, *PhRvL*, **90**, 241102
- Lattimer, J., & Swesty, F. D. 1991, *NuPhA*, **535**, 331

- Liebendörfer, M., Messer, O. E. B., Mezzacappa, A., et al. 2004, [ApJS](#), **150**, 263
- Liebendörfer, M., Mezzacappa, A., Thielemann, F.-K., et al. 2001, *PhRvD*, **63**, 103004
- Marek, A., Dimmelmeier, H., Janka, H.-T., Müller, E., & Buras, R. 2006, [A&A](#), **445**, 273
- Marek, A., & Janka, H.-T. 2009, [ApJ](#), **694**, 664
- Mezzacappa, A. 2005, *ARNPS*, **55**, 467
- Mezzacappa, A., Calder, A. C., Bruenn, S. W., et al. 1998, [ApJ](#), **495**, 911
- Mezzacappa, A., Liebendörfer, M., Messer, O. E., et al. 2001, *PhRvL*, **86**, 1935
- Müller, B., Janka, H.-T., & Heger, A. 2012a, [ApJ](#), **761**, 72
- Müller, B., Janka, H.-T., & Marek, A. 2012b, [ApJ](#), **756**, 84
- Müller, B., Janka, H.-T., & Marek, A. 2013, [ApJ](#), **766**, 43
- Müller, E., & Steinmetz, M. 1995, *CoPhC*, **89**, 45
- Murphy, J. W., & Burrows, A. 2008, [ApJ](#), **688**, 1159
- O'Connor, E., & Ott, C. D. 2011, [ApJ](#), **730**, 70
- Rampp, M., & Janka, H.-T. 2000, [ApJL](#), **539**, L33
- Reddy, S., Prakash, M., & Lattimer, J. M. 1998, *PhRvD*, **58**, 013009
- Scheck, L., Kifonidis, K., Janka, H.-T., & Müller, E. 2006, [A&A](#), **457**, 963
- Smartt, S. J. 2009, [ARA&A](#), **47**, 63
- Suwa, Y., Takiwaki, T., Whitehouse, S. C., Liebendörfer, M., & Sato, K. 2010, *PASJ*, **62**, L49
- Takiwaki, T., Kotake, K., & Suwa, Y. 2012, [ApJ](#), **749**, 98
- Thompson, T. A., Quataert, E., & Burrows, A. 2005, [ApJ](#), **620**, 861
- Woosley, S. E., & Heger, A. 2007, *PhR*, **442**, 269
- Woosley, S. E., Wilson, J. R., Mathews, G. J., Hoffman, R. D., & Meyer, B. S. 1994, [ApJ](#), **433**, 229